RSC Advances

PAPER

Cite this: *RSC Adv.*, 2022, **12**, 11272

Enhanced hydrogen storage properties of $ZrTiVAl_{1-x}Fe_x$ high-entropy alloys by modifying the Fe content

Xiangfeng Ma,[a] Xin Ding,*[b] Ruirun Chen,*[a] Xuefeng Gao,[b] Yanqing Su[b] and Hongzhi Cui[a]

Lightweight ZrTiVAl high-entropy alloys have shown great potential as a hydrogen storage material due to their appreciable capacity, easy activation, and fast hydrogenation rates. In this study, transition metal Fe was used to improve the hydrogen storage properties of the equimolar ZrTiVAl alloy, and $ZrTiVAl_{1-x}Fe_x$ (x = 0, 0.2, 0.4, 0.6, 0.8, 1) alloys were prepared to investigate the microstructure evolution and hydrogen storage properties. The results show that the $ZrTiVAl_{1-x}Fe_x$ alloys are composed of a C14 Laves phase and Ti-rich HCP phase. With Fe substituting Al, the fraction of the C14 Laves phase increases and that of the HCP phase decreases. Besides, the interdendritic area fraction reaches the maximum when the Fe ratio is 0.2. The element V transferred to the C14 Laves phase from the HCP phase, which is caused by the strong affinity between V and Fe. The $ZrTiVAl_{1-x}Fe_x$ alloys show enhanced hydrogenation kinetics and capacities. Notably, the ZrTiVFe alloy can reversely absorb 1.58 wt% hydrogen even at room temperature under 1 MPa H_2. The reduced interdendritic phase is beneficial to shorten the H atom diffusion distance, thus improving the hydrogenation rates. Both the transfer of the hydrogen-absorbing element V to the C14 Laves phase and the increased fraction of the C14 Laves phase lead to the increase of hydrogen storage capacity with the addition of Fe. Moreover, the increased Fe content leads to an increase of average valence electron concentration (VEC), where a larger VEC destabilizes the hydrides, and the desorption temperature of $ZrTiVAl_{1-x}Fe_x$ hydride decreases significantly.

Received 17th February 2022
Accepted 3rd April 2022

DOI: 10.1039/d2ra01064j

rsc.li/rsc-advances

1. Introduction

The energy crisis has become a serious problem that has to be faced due to the rapid consumption of fossil fuels.[1,2] In contrast, hydrogen energy is considered as a potential energy solution due to its cleanliness, renewable nature and high energy density.[3–5] However, the safe and efficient storage makes the widespread use of hydrogen difficult.[6,7] Metal hydrides can serve as a good container for hydrogen storage due to their safety and high hydrogen storage capacity.[8–11] Therefore, it is particularly important to develop excellent hydrogen storage materials with metal hydrides as carriers.

The concept of high-entropy alloys or multi-component alloys, which are composed of multiple principal elements, was first proposed by Yeh *et al.* and Cantor *et al.* in 2004.[12,13] High-entropy alloys have the characteristics of high entropy, severe lattice distortion, slow diffusion and cocktail effect, thus high-entropy alloys exhibit ultra-high fracture toughness,[14] excellent specific strength,[15] outstanding superconductivity,[16] and significant corrosion resistance.[17] This concept provides a new strategy for material design. Since the severe lattice distortion of high-entropy alloys can provide more favorable interstitial positions for hydrogen atoms,[18,19] high-entropy alloys are considered to be excellent hydrogen storage materials.

Recently, high-entropy alloys are emerging as a new category of hydrogen storage materials, and their hydrogen storage capacity,[20] kinetics,[21] thermodynamics,[22] activation properties,[23] and cycling performance[24] are being investigated. In previous studies,[20–30] high-entropy hydrogen storage alloys are basically divided into two types: Laves phase hydrogen storage alloys[25–28] and BCC solid solution hydrogen storage alloys.[29–31] These two types of alloys have different advantages. The high-entropy alloys with Laves phase structure have the advantages of easy activation and fast kinetics.[25,26] The high-entropy alloys of BCC solid solution have relatively high hydrogen storage capacity, and the phase structure of such alloys usually transforms to generate hydrides of FCC structure during hydrogenation.[20,29] Currently, for Laves phase high entropy alloys, it is very important to improve the hydrogen storage capacity and desorption properties of the alloy to approach practical applications.

[a]*School of Materials Science and Engineering, Shandong University of Science and Technology, Qingdao 266500, PR China. E-mail: ruirunchen@hit.edu.cn; Fax: +86-451-86412394; Tel: +86-451-86412394*

[b]*National Key Laboratory for Precision Hot Processing of Metals, Harbin Institute of Technology, Harbin 150001, PR China. E-mail: dingxin_hit@hit.edu.cn*

In this study, the alloy samples contained Zr, Ti, and V elements, which all have high hydrogen storage capacity. To these alloy samples, the element Al and the element Fe were added to form $ZrTiVAl_{1-x}Fe_x$ (x = 0, 0.2, 0.4, 0.6, 0.8, 1) high entropy alloys. Theoretically, the addition of light element Al may be beneficial to produce new lightweight alloys that can absorb hydrogen with improved gravimetric storage capacities. The addition of transition element Fe with a larger VEC value may improve the desorption performance of the alloy, and the addition of Fe reduces the cost of hydrogen storage alloys, which is more conducive to meet practical applications. The purpose of this study is to investigate the effects of Al and Fe on the microstructure and hydrogen storage properties of alloys, and to reveal the changing mechanism of hydrogen storage properties, so as to obtain a high entropy alloy with excellent hydrogen storage properties.

2. Experimental methods

2.1 High-entropy alloy fabrication

The purity of raw materials (Zr, Ti, V, Al and Fe) used in this work were all higher than 99.5%. Alloys with a nominal composition of $ZrTiVAl_{1-x}Fe_x$ (x = 0, 0.2, 0.4, 0.6, 0.8, 1) were synthesized by using the arc-melting method in a water-cooled copper crucible. The smelting process took place under the protection of argon atmosphere. Each alloy ingot weighs about 120 g. The mass of each metal is shown in Table 1. The V, Zr metals with higher melting temperature were put on the top layer, while the Ti, Fe, Al metals with lower melting temperature were put on the bottom layer. After the arc current slowly increased to 600 A, melting temperature was around 2000 °C. And the melted Zr, Ti, V, Al, and Fe metals were mixed to form an alloy ingot. The alloy ingots were rotated and remelted five times to improve the compositional homogeneity.

2.2 Sample characterization

The crystalline structures of $ZrTiVAl_{1-x}Fe_x$ alloys were characterized by X-ray diffraction (XRD). Before XRD analysis, 1000# sandpaper was used to polish and remove the oxide layer from the surface. The X-ray diffractometer model is Empyrean. The test conditions were: copper target radiation (Cu-Kα ray, λ = 0.15405 nm) was used, the test angle was 20–100°, and the test step size was 4 degrees per min. Samples were prepared for microstructure analysis by polishing with 3000# sandpaper. The microstructures of $ZrTiVAl_{1-x}Fe_x$ alloys were acquired by a SUPRA55 field emission scanning electron microscopy (SEM).

Table 1 Mass of each metal in $ZrTiVAl_{1-x}Fe_x$ alloy

Alloy	Zr (g)	Ti (g)	V (g)	Al (g)	Fe (g)
$x = 0$	50.43	26.47	28.17	14.93	0
$x = 0.2$	49.13	25.79	27.44	11.63	6.01
$x = 0.4$	47.89	25.14	26.74	8.50	11.73
$x = 0.6$	46.71	24.52	26.08	5.53	17.16
$x = 0.8$	45.58	23.93	25.46	2.70	22.33
$x = 1$	44.52	23.37	24.86	0	27.25

The elemental distributions of Zr, Ti, V, Al, and Fe elements were determined by energy dispersive spectroscopy (EDS). To study hydrogen desorption behaviors of hydrogenated samples, powder samples with a mass of approximately 20 mg were placed in Al_2O_3 crucible and subjected to differential scanning calorimetry (DSC) measurements from room temperature (RT) to 700 °C at a heating rate of 5 °C. The equipment model is the German Netzsch STA 449F3. To reduce the severe oxidation of the $ZrTiVAl_{1-x}Fe_x$ hydride powders, the DSC tests were carried out in an inert argon gas flowing environment.

2.3 Sample hydrogenation

Samples for dehydrogenation/hydrogenation testing were taken from the core of each ingot. Prior to isothermal dehydrogenation testing, the bulk samples were mechanically cut, and then pulverized to less than 200 mesh using a planetary high energy ball mill (HEBM) with a 50 mL stainless steel sealed vial. The weight ratio of ball to powder was 10 : 1. The ball-milling process was performed under the protection of high purity argon (purity 99.999%) at a rotate speed of 100 rpm for 2 h. Before the performance testing, $ZrTiVAl_{1-x}Fe_x$ samples were activated by three de-/hydrogenation cycles at 200 °C under 1 MPa hydrogen pressure. The hydrogenation process of the $ZrTiVAl_{1-x}Fe_x$ powder samples was carried out using a precise volumetric Sieverts-type apparatus, and the purity of hydrogen gas is 99.999%. Before the second hydrogenation of the samples, the samples were desorbed again under vacuum at 400 °C for one hour in order to ensure the complete desorption of hydrogen. To avoid oxidation of powder samples, all operations were performed in a glove box.

3. Results

3.1 Structural characterization of $ZrTiVAl_{1-x}Fe_x$

The XRD patterns of $ZrTiVAl_{1-x}Fe_x$ (x = 0, 0.2, 0.4, 0.6, 0.8, 1) alloy samples are shown in Fig. 1. The phase composition does not change significantly as the Fe element gradually replaces the Al element. The major diffraction peaks of the $ZrTiVAl_{1-x}Fe_x$ alloys are identified to C14 Laves phase which crystallizes in the hexagonal ($MgZn_2$ type) structure with space group $P6_3/mmc$. Beside the C14 Laves phase, a small amount of HCP phase is also present. In addition, the diffraction peaks of the C14 Laves phase shift to the higher scattering angle, while the diffraction peaks of the HCP phase shift toward an opposite direction. It indicates a decrease of lattice constants for the C14 Laves phase and an increase for the HCP phase.[32] It may be related to the smaller radius of Fe than that of Al.

The SEM backscattered electron images of the $ZrTiVAl_{1-x}Fe_x$ (x = 0, 0.2, 0.4, 0.6, 0.8, 1) alloy samples are shown in Fig. 2. It can be clearly seen that the $ZrTiVAl_{1-x}Fe_x$ alloys are mainly composed of two phases, which is consistent with the result of XRD. Typical dendritic and interdendritic structures (define as DR and ID, respectively) are observed in the $ZrTiVAl_{1-x}Fe_x$ alloys. Combined with the XRD results, the light area is the C14 Laves phase, the dark area is the HCP phase. The DR areas of the $ZrTiVAl_{1-x}Fe_x$ alloys are C14 Laves phase. With Fe replacing

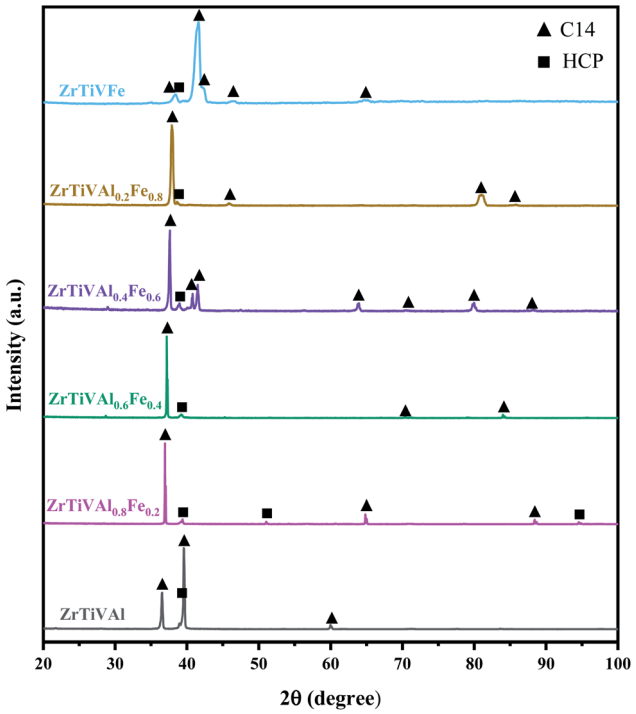

Fig. 1 X-ray diffraction patterns of $ZrTiVAl_{1-x}Fe_x$ (x = 0, 0.2, 0.4, 0.6, 0.8, 1) alloy samples.

Al gradually, the ID structure changes from the two phases of C14 Laves and HCP phase to a single HCP phase, and the ID area fraction increases and then decreases. The area fraction of each phase was calculated by Imagin-Pro software. Table 2 displays the phase fraction of the phases for the $ZrTiVAl_{1-x}Fe_x$ alloys. With the increase of Fe content, the phase fraction of C14 Laves increases while that of HCP decreases.

The EDS maps of the $ZrTiVAl_{1-x}Fe_x$ (x = 0, 0.6, 1) alloy samples are shown in Fig. 3, which reveal the elemental distribution between the two phases. These show that the dark area (the HCP phase) is rich in Ti, while the light area (the C14 Laves phase) is rich in Zr, Fe and Al. The Ti element segregation can be explained by the mixing enthalpies among the principal metallic elements.[32] It is worth noting that the distribution of V element changes significantly. As Fe gradually replaces Al, V element changes from evenly distribution to enrichment in the C14 Laves phase.

Table 2 The phase fraction of the phases for $ZrTiVAl_{1-x}Fe_x$ alloys

Phase	$x = 0$	$x = 0.2$	$x = 0.4$	$x = 0.6$	$x = 0.8$	$x = 1$
C14	30.40%	22.40%	14.50%	11.80%	8.10%	5.60%
HCP	69.60%	77.60%	85.50%	88.20%	91.90%	94.40%

3.2 Hydrogenation of $ZrTiVAl_{1-x}Fe_x$

Since the hydrogen storage properties of the novel $ZrTiVAl_{1-x}Fe_x$ alloy is not clear, to evaluate whether the alloy needs activation, the first three hydrogenation curves were carried out at a medium temperature of 200 °C. Moreover, to evaluate the effect of different temperatures on the hydrogenation behavior of the $ZrTiVAl_{1-x}Fe_x$ alloy, the isothermal kinetic curves of the alloy were measured at RT, 150 °C and 300 °C sequentially. In order to evaluate the hydrogenation behavior of the alloy with the best composition at different pressures, its isothermal kinetic curves were measured at 0.2 Mpa, 0.5 Mpa and 1 MPa, respectively.

At 200 °C and 1 MPa hydrogen pressure, three cycles of de-/hydrogenation were carried out for $ZrTiVAl_{1-x}Fe_x$ (x = 0, 0.2, 0.4, 0.6, 0.8, 1). Hydrogenation kinetic curves in the first three cycles (1st, 2nd, 3rd) are shown in Fig. 4(a), (b) and (c), respectively.

During the 1st hydrogenation process, the alloys except $ZrTiVAl_{0.8}Fe_{0.2}$ absorb hydrogen extremely fast in less than a minute, exhibit rapid hydrogen chemisorption kinetics. The relatively gentle hydrogenation process of $ZrTiVAl_{0.8}Fe_{0.2}$ is probably related to its wide interdendritic region.[33] The ZrTiVFe alloy has the largest hydrogen storage capacity, which is

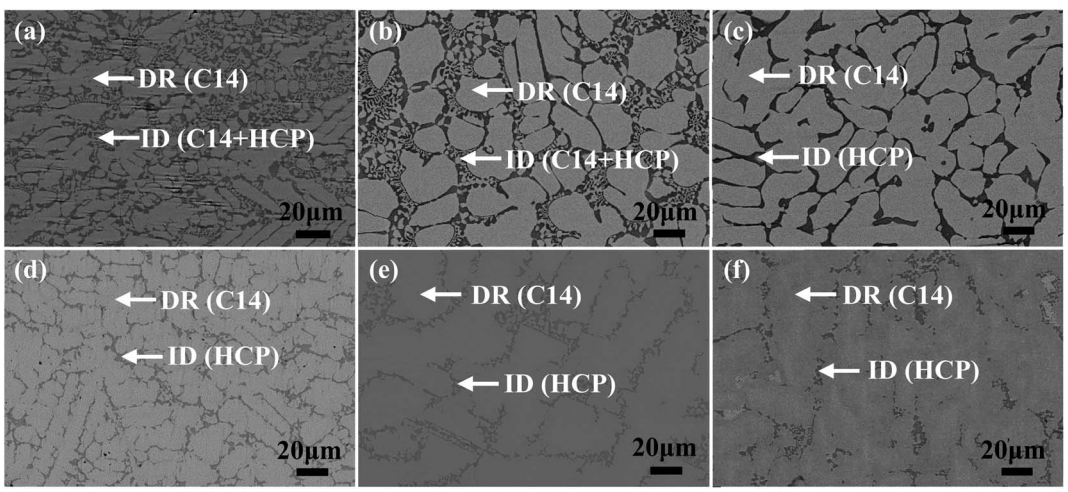

Fig. 2 SEM backscattered electron images (a–f) of $ZrTiVAl_{1-x}Fe_x$ (x = 0, 0.2, 0.4, 0.6, 0.8, 1) alloy samples.

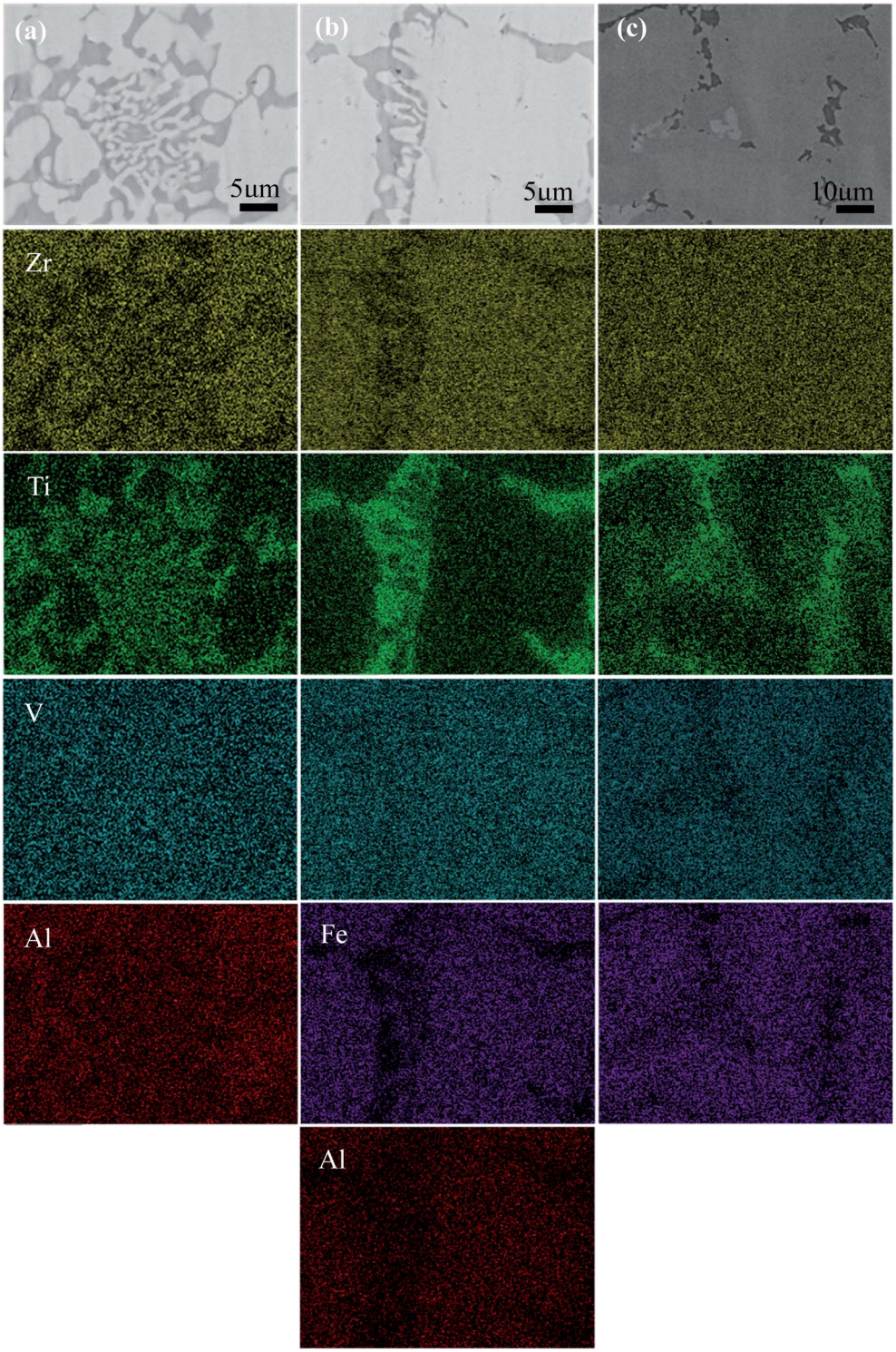

Fig. 3 The EDS maps (a–c) of the $ZrTiVAl_{1-x}Fe_x$ ($x = 0$, 0.6, 1) alloy samples.

1.67 wt%. While the ZrTiVAl alloy has the smallest hydrogen storage capacity, which is 1.4 wt%. After complete dehydrogenation (complete dehydrogenation refers to the state after one hour of dehydrogenation under vacuum at 400 °C in this study), $ZrTiVAl_{1-x}Fe_x$ alloys undergo a second hydrogenation. All alloys have fast hydrogen chemisorption kinetics, and the hydrogen storage within 3 minutes reaches more than 95% of the maximum hydrogen storage. The maximum hydrogen storage capacity of all alloys decreases. This is related to the fact that part of the hydrogen cannot be desorbed under vacuum at 400 °C. The maximum hydrogen storage of ZrTiVFe is reduced to 1.3 wt%. During the third hydrogenation process, the

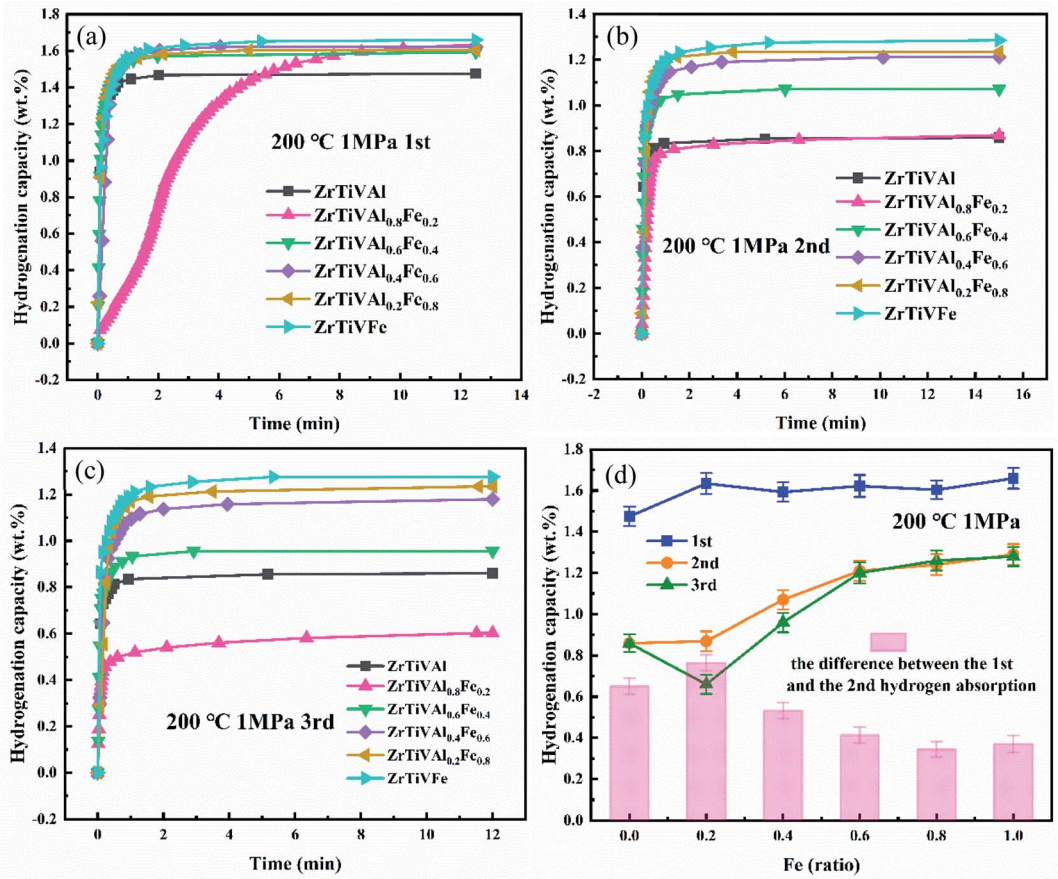

Fig. 4 Hydrogenation kinetic curves in the first three cycles (a–c) and maximum hydrogen storage (d) of $ZrTiVAl_{1-x}Fe_x$ ($x = 0$, 0.2, 0.4, 0.6, 0.8, 1) alloy powders at 200 °C under 1 MPa hydrogen pressure.

maximum hydrogen storage capacity of alloys $ZrTiVAl_{0.8}Fe_{0.2}$ and $ZrTiVAl_{0.6}Fe_{0.4}$ decreases again. The maximum hydrogen storage capacity of other alloys is basically unchanged.

As Fe gradually replaces Al, the maximum hydrogen storage of $ZrTiVAl_{1-x}Fe_x$ is shown in Fig. 4(d). The ZrTiVAl alloy has the smallest hydrogen storage capacity in the 1st hydrogenation, which indicates that the light element Al has no positive effect on the hydrogen storage capacity in the $ZrTiVAl_{1-x}Fe_x$ alloys. The difference between the 1st and the 2nd hydrogenation represents the amount of hydrogen that is difficult to desorb. It can be seen from Fig. 4(d) that the addition of the element Fe has a positive effect on the hydrogen desorption of $ZrTiVAl_{1-x}Fe_x$ series alloys.

In order to illustrate the hydrogen storage capacity of $ZrTiVAl_{1-x}Fe_x$ ($x = 0$, 0.2, 0.4, 0.6, 0.8, 1) alloys at different temperatures, hydrogenation tests were performed on the alloys at RT, 150 °C and 300 °C. Hydrogenation kinetic curves of $ZrTiVAl_{1-x}Fe_x$ at RT, 150 °C and 300 °C are shown in Fig. 5(a), (b) and (c), respectively.

From Fig. 5(a), it can be seen that all alloys except $ZrTiVAl_{0.8}Fe_{0.2}$ have fast hydrogenation kinetics at RT. The hydrogen atom diffusion rate is low at RT, which suggests that the hydrogen atom diffusion rate in these alloys is not a key factor affecting the kinetics of hydrogen chemisorption. It is worth noting that ZrTiVFe alloy has the largest hydrogen storage capacity, which is 1.58 wt%. However, for $ZrTiVAl_{0.8}Fe_{0.2}$ alloy, the hydrogen atom diffusion rate has an effect on its hydrogenation kinetics. As the temperature increases, the hydrogen atom diffusion rate increases. The hydrogenation kinetics of $ZrTiVAl_{0.8}Fe_{0.2}$ alloy at 150 °C and 300 °C are significantly improved compared with room temperature.[22]

Fig. 5(d) shows the change in the maximum hydrogen storage of different alloy compositions with temperature. As the temperature increases, the maximum hydrogen storage of all alloys except $ZrTiVAl_{0.8}Fe_{0.2}$ decreases, this is because the chemisorption of hydrogen is an exothermic reaction.[22] However, the maximum hydrogen storage capacity of $ZrTiVAl_{0.8}Fe_{0.2}$ alloy increases first and then decreases with increasing temperature, which is attributed to the wide interdendritic eutectic structure.

To study the hydrogen storage capacity of the optimal composition ZrTiVFe alloy at room temperature and low pressure, hydrogenation experiments were carried out at 1, 0.5, and 0.2 MPa. Hydrogenation kinetic curves of ZrTiVFe alloy at RT under different hydrogen pressure are shown in Fig. 6(a).

It can be seen from Fig. 6(a) that the maximum hydrogen storage capacity decreases with the decrease of the hydrogen pressure. The ZrTiVFe alloy has a maximum hydrogen storage

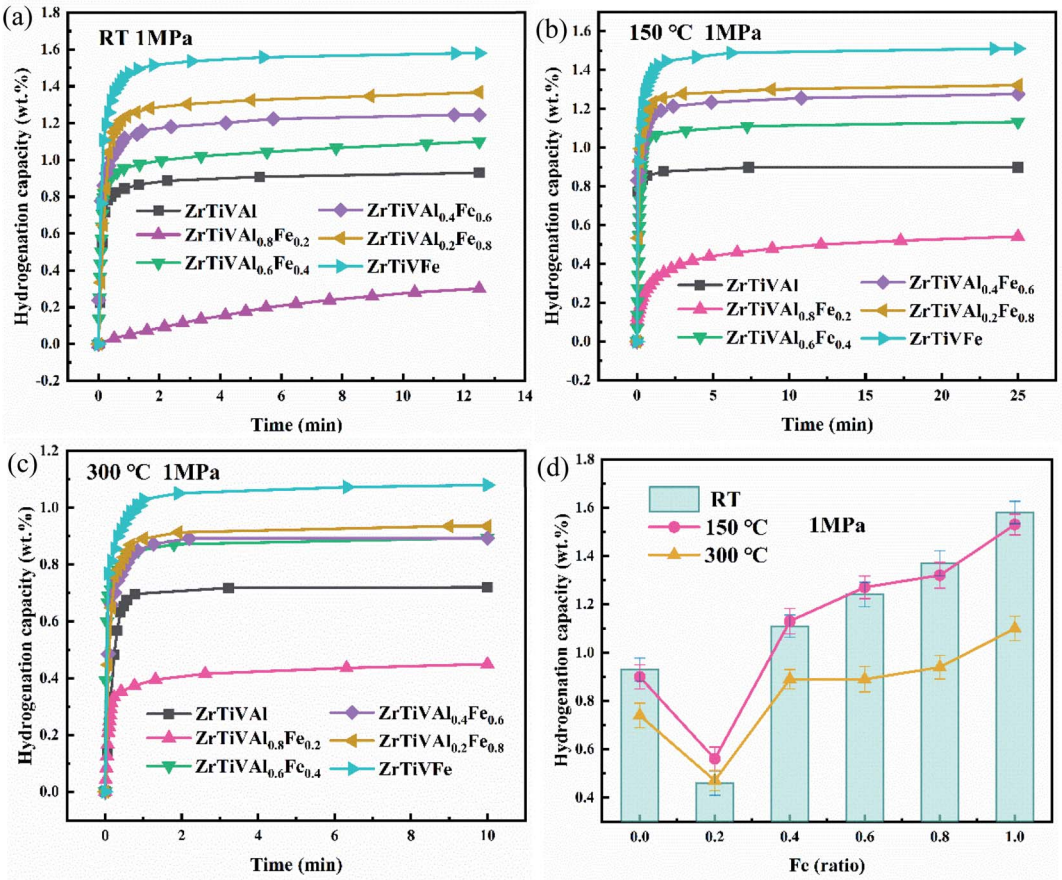

Fig. 5 Hydrogenation kinetic curves (a–c) and comparison of hydrogen storage (d) of $ZrTiVAl_{1-x}Fe_x$ (x = 0, 0.2, 0.4, 0.6, 0.8, 1) alloy powders at different temperature under 1 MPa hydrogen pressure.

capacity of 1.54 wt% and 1.38 wt% at RT under 0.5 Mpa and 0.2 MPa hydrogen pressure, respectively. It is worth noting that the hydrogenation kinetics of the ZrTiVFe alloy decreases significantly under 0.2 MPa hydrogen pressure and also slightly decreases under 0.5 MPa hydrogen pressure. The hydrogenation kinetic behavior of ZrTiVFe alloy at different temperatures is shown in Fig. 6(b). As the temperature increases, the maximum hydrogen storage capacity of ZrTiVFe alloy decreases. But no matter in low, medium or high temperature, ZrTiVFe alloy has fast hydrogen chemisorption kinetics.

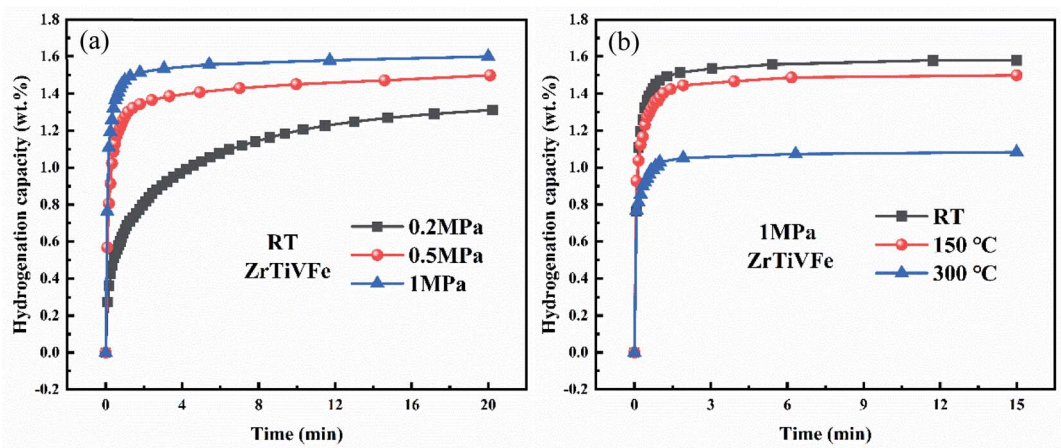

Fig. 6 Hydrogenation kinetic curves of ZrTiVFe alloy powders at RT under different hydrogen pressure (a) and at different temperature under 1 MPa hydrogen pressure (b).

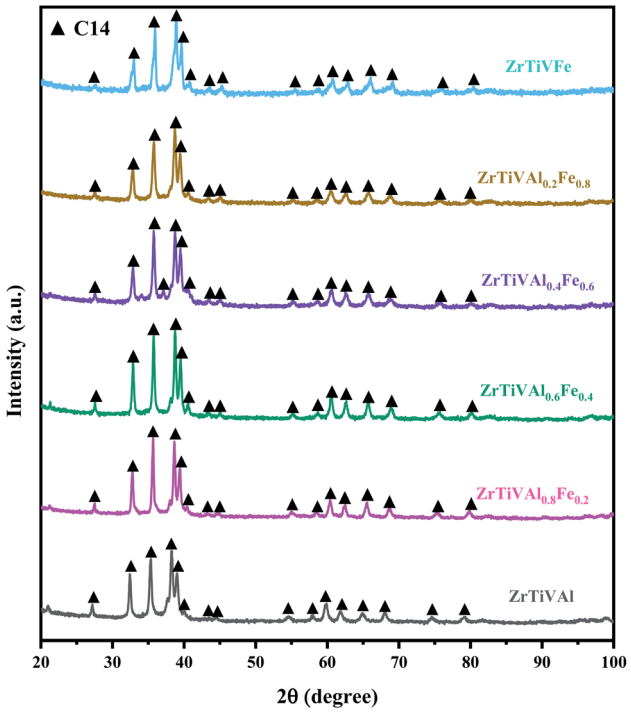

Fig. 7 X-ray diffraction patterns of $ZrTiVAl_{1-x}Fe_x$ (x = 0, 0.2, 0.4, 0.6, 0.8, 1) alloy powders after hydrogenation.

3.3 Crystalline structure of $ZrTiVAl_{1-x}Fe_x$ after hydrogenation

To study the change of the crystalline structure of $ZrTiVAl_{1-x}Fe_x$ (x = 0, 0.2, 0.4, 0.6, 0.8, 1) after hydrogen storage, the XRD test was performed on the $ZrTiVAl_{1-x}Fe_x$ powder samples after hydrogen storage. The XRD patterns of the $ZrTiVAl_{1-x}Fe_x$ powder samples after hydrogenation are shown in Fig. 7.

The $ZrTiVAl_{1-x}Fe_x$ powder samples have single C14 Laves phase crystalline structure after hydrogenation tests. Compared with the XRD patterns before hydrogenation, few HCP phases are observed because of the low HCP content. The H atoms are stored in the interstices of the lattice. The crystalline structure of $ZrTiVAl_{1-x}Fe_x$ remains unchanged after hydrogen storage, which is consistent with previous research.[25]

3.4 Hydrogen desorption of $ZrTiVAl_{1-x}Fe_x$

The hydrogen desorption behaviours of hydrogenated $ZrTiVAl_{0.8}Fe_{0.2}$, $ZrTiVAl_{0.6}Fe_{0.4}$, $ZrTiVAl_{0.2}Fe_{0.8}$ and ZrTiVFe alloys were also studied by DSC under inert gas (Ar) with a heating rate of 5 °C min^{-1} from RT to 700 °C. The DSC curves during desorption of hydrogen are shown in Fig. 8.

For the $ZrTiVAl_{0.8}Fe_{0.2}H_y$, $ZrTiVAl_{0.6}Fe_{0.4}H_y$, $ZrTiVAl_{0.2}Fe_{0.8}$-H_y and $ZrTiVFeH_y$ phases, the desorptions consist of three events. The first endothermic peaks of $ZrTiVAl_{1-x}Fe_x$ (x = 0.2, 0.4, 0.8, 1) are detected at around 62 °C. Intense endothermic peaks of $ZrTiVAl_{1-x}Fe_x$ (x = 0.2, 0.4, 0.8, 1) are observed around 475, 390, 380 and 322 °C, respectively, which is the typical desorption of hydrogen from metal hydrides. The small endothermic peaks of $ZrTiVAl_{1-x}Fe_x$ (x = 0.2, 0.4, 0.8, 1) are detected at 556, 504, 459 and 403 °C, respectively.

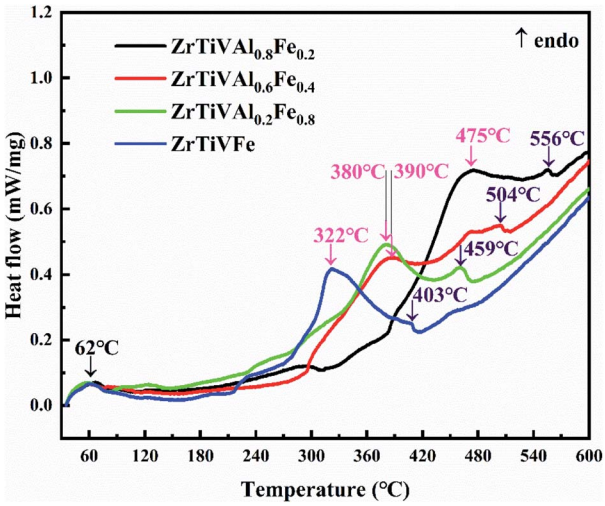

Fig. 8 DSC measurements during hydrogen desorption from $ZrTiVAl_{0.8}Fe_{0.2}H_x$, $ZrTiVAl_{0.6}Fe_{0.4}H_x$, $ZrTiVAl_{0.2}Fe_{0.8}H_x$ and $ZrTiVFeH_x$ at a constant heating-rate of 5 °C min^{-1} from RT to 700 °C.

The C14 structure has three types of tetrahedral interstitial sites: A_2B_2 sites, A_1B_3 sites, and B_4 site. The A_2B_2 site has the largest gap size, while the B_4 site has the smallest gap size. It is well known that hydrogen atoms stored in a small gap are easy to desorb. The endothermic peaks at different temperatures are speculated to be related to hydrogen desorption at different interstitial sites. The decrease of the phase transition temperature reflects the decrease of the temperature at which the desorption reaction occurs, which proves that the desorption performance of the alloy is improved. It is worth noting that the temperature of the desorption peak gradually decreases with Fe replacing Al gradually, which indicates that the addition of the element Fe has a positive effect on the desorption of the alloy.

4. Discussions

In this study, a series of $ZrTiVAl_{1-x}Fe_x$ (x = 0, 0.2, 0.4, 0.6, 0.8, 1) high-entropy alloys were prepared by arc melting, the alloys are composed of C14 Laves phase and HCP phase. The $ZrTiVAl_{1-x}Fe_x$ alloys have excellent hydrogen storage performance, especially fast hydrogen chemisorption kinetics. The δr (atomic size mismatch), $\Delta\chi_{Allen}$ (Allen electronegativity difference) and VEC (average valence electron concentration) parameters of high-entropy alloys affect phase formation[34] and hydrogen storage properties.[29,30,35] Equations for these terms are

$$\delta r = 100\% \sqrt{\sum c_i (1 - r_i/\bar{r})^2} \quad (1)$$

$$\Delta\chi_{Allen} = 100\% \sqrt{\sum c_i (1 - \chi_{iAllen}/\chi_a)^2} \quad (2)$$

$$VEC = \sum c_i VEC_i \quad (3)$$

Here r_i, χ_i and VEC_i are atomic radius, electronegativity and valence electron concentration of element i; c_i is the atom fractions of atom i; $\bar{r}$ ($=\sum c_i r_i$) and χ_a ($=\sum c_i \chi_i$) are the average

Table 3 Atomic radii, Allen electronegativity and VEC for elements

Element	r [Å]	χ_{Allen} [∅]	VEC [∅]
Zr	1.60	1.32	4
Ti	1.46	1.38	4
V	1.32	1.53	5
Al	1.43	1.613	3
Fe	1.24	1.80	8

Table 4 The δr, $\Delta\chi_{Allen}$ and VEC parameters calculated for the $ZrTiVAl_{1-x}Fe_x$ ($x = 0$, 0.2, 0.4, 0.6, 0.8, 1) alloys

Alloy	δr/%	$\Delta\chi_{Allen}$/%	VEC
$x = 0$	6.87	7.98	4
$x = 0.2$	7.63	9.15	4.25
$x = 0.4$	8.28	10.12	4.5
$x = 0.6$	8.84	10.95	4.75
$x = 0.8$	9.34	11.67	5
$x = 1$	9.78	13.85	5.25

atomic radius and electronegativity. Table 3 shows the atomic radii, Allen electronegativity and VEC values of different elements.[36–38]

The parameters of δr, $\Delta\chi_{Allen}$ and VEC were calculated in Table 4. In the previous study,[34] the criteria for the Laves phase were obtained as $\delta r > 5.0\%$ and $\Delta\chi_{Allen} > 7.0\%$, which is consistent with the results of this study. With Fe replacing Al gradually, the value of the parameters δr and $\Delta\chi_{Allen}$ increases, and the tendency to form Laves phase increases. The increase of the element Fe leads to the increase of the VEC value. Nygård *et al.*[35] reported that a larger VEC destabilizes the hydrides. From the DSC results, it has a positive effect on the desorption property, which is also consistent with previous research.

The fast hydrogen chemisorption kinetic of $ZrTiVAl_{1-x}Fe_x$ alloys can be related to the lattice defects caused by the lattice distortion.[19,21] It is generally believed that high-entropy alloys suffer from serious lattice distortion due to the different atomic sizes of multiple elements. Lattice defects contribute to the nucleation of hydrides. A higher δr value represents a higher degree of lattice distortion.[29] Schematic diagram for diffusion of H atoms in ZrTiVFe and $ZrTiVAl_{0.8}Fe_{0.2}$ alloys are shown in Fig. 9. The HCP phase is a brittle phase that acts as a diffusion channel, which has a positive effect on the diffusion of hydrogen atoms. This is the reason why $ZrTiVAl_{1-x}Fe_x$ alloys have fast hydrogen chemisorption kinetics even at room temperature. However, compared with other alloys, the $ZrTiVAl_{0.8}Fe_{0.2}$ alloy absorbs hydrogen relatively slowly at room temperature due to the wide interdendritic eutectic phase that lengthens the diffusion path of hydrogen. And the small amount of interdendritic C14 phase that can absorb hydrogen acting as a suppressor of hydrogen diffusion.

The maximum hydrogen storage capacity of the ZrTiVFe alloy is 1.58 wt% at RT under 1 MPa hydrogen pressure. It is worth noting that the hydrogen storage capacity reaches 1.51 wt% in only two minutes, which is attributed to the high δr. The mixing enthalpies of V and Al, Fe, Zr and Ti are −16, −7, −4 and −2 kJ mol^{-1}, respectively.[39] It can be seen that V has the highest affinity with Al, while V has the lowest affinity with Ti.[40] The decreased Al content causes the V element to be transferred to the Zr, Fe-rich C14 Laves phase. As Fe gradually replaces Al, the maximum hydrogen storage capacity increases, which is

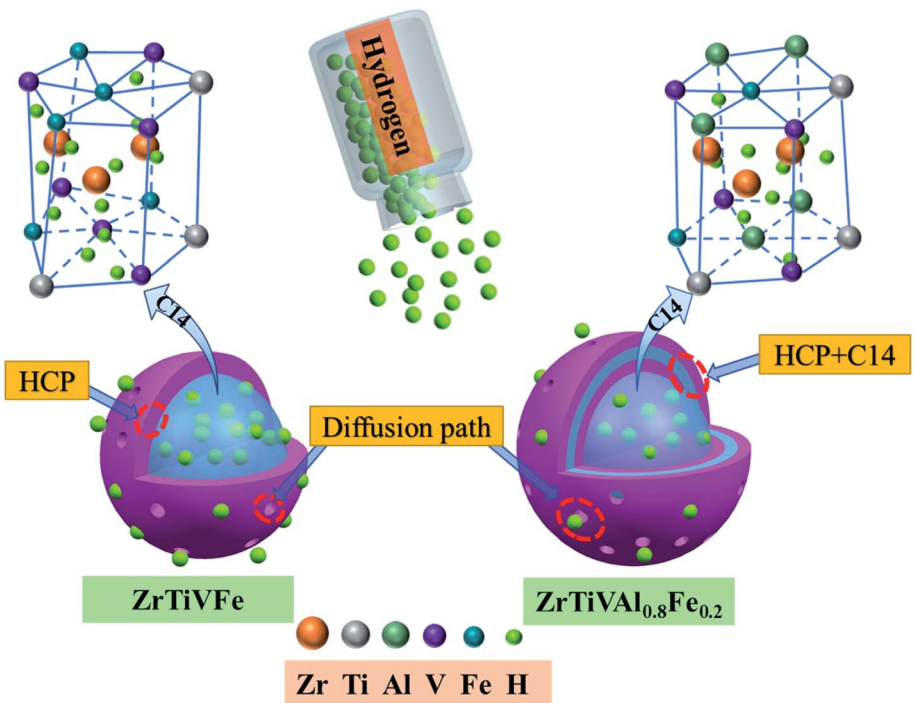

Fig. 9 Schematic diagram for diffusion of H atoms in ZrTiVFe and $ZrTiVAl_{0.8}Fe_{0.2}$ alloys.

mainly attributed to the transfer of the strongly hydrogen-absorbing element V from the HCP phase to the C14 Laves phase and the increase in the fraction of the C14 Laves phase.

5. Conclusions

In this study, a series of novel $ZrTiVAl_{1-x}Fe_x$ ($x = 0$, 0.2, 0.4, 0.6, 0.8, 1) high-entropy alloys for hydrogen storage were synthesized by metallurgy methods. Their microstructure features and hydrogen de-/hydrogenation properties were studied in detail. The main conclusions can be drawn as follows:

(1) $ZrTiVAl_{1-x}Fe_x$ high entropy alloys are mainly composed of C14 Laves phase and HCP phases. Due to the severe lattice distortion and friable HCP interdendritic phase, the $ZrTiVAl_{1-x}Fe_x$ alloys exhibited the rapid hydrogen chemisorption kinetics even at room temperature. With Fe replacing Al completely, the ZrTiVFe alloy can absorb 1.58 wt% hydrogen even at room temperature under 1 MPa hydrogen pressure. Notably, the ZrTiVFe alloy can still absorb 1.38 wt% hydrogen at the lower hydrogen pressure of 0.2 MPa.

(2) With Fe replacing Al gradually, interdendritic area increases and then decreases. The interdendritic region serves as the diffusion channel for hydrogen. The diffusion path is first lengthened and then shortened, and the hydrogenation rate first decreases and then increases.

(3) With Fe replacing Al, the phase fraction of C14 Laves increases. And the hydrogen-absorbing element V gradually transfers to the main hydrogen storage phase, namely the C14 Laves phase, which are the key factor that increasing the hydrogen storage capacity.

(4) The element Fe shows a strong catalytic effect on lowering the hydrogen desorption temperature of ZrTiVAl alloy. The increase of the element Fe leads to the increase of the VEC value, a larger VEC value destabilizes the hydrides. Therefore, the desorption temperature of $ZrTiVAl_{1-x}Fe_x$ hydride drops significantly with Fe replacing Al. Moreover, according to DCS thermodynamic analysis, it can be known that the hydrogen desorption property of the alloy is closely related to the phase composition and size of the interdendritic region.

Conflicts of interest

The authors declare that they have no known competing financial interests or personal relationships that could have appeared to influence the work reported in this paper.

Acknowledgements

This work was supported by National Key Research and Development Program of China (2017YFA0403802), the National Natural Science Foundation of China (No. 51825401) and Heilongjiang Postdoctoral Fund (LBH-Z20056).

References

1 X. B. Yu, Z. W. Tang, D. L. Sun, L. Z. Ouyang and M. Zhu, Recent advances and remaining challenges of nanostructured materials for hydrogen storage applications, *Prog. Mater. Sci.*, 2017, **88**, 1–48, DOI: **10.1016/j.pmatsci.2017.03.001**.

2 U. Eberle, M. Felderhoff and F. Schuth, Chemical and physical solutions for hydrogen storage, *Angew. Chem., Int. Ed.*, 2009, **48**, 6608–6630, DOI: **10.1002/anie.200806293**.

3 L. Schlapbach and A. Züttel, Hydrogen-storage materials for mobile applications, *Nature*, 2001, **414**, 353–358, DOI: **10.1038/35104634**.

4 Y. Yin, Y. H. Qi, B. Li, H. Gu, J. H. Zhao, L. Q. Ji, B. Zhang, Z. M. Yuan and Y. H. Zhang, A catalytic mechanism investigation of TiF_3 on hydriding/dehydriding properties of $Mg_{85}Cu_5Ni_{10}$ alloy, *RSC Adv.*, 2021, **11**, 8940–8950, DOI: **10.1039/d0ra10224e**.

5 A. Züttel, Materials for hydrogen storage, *Mater. Today*, 2003, **6**, 24–33, DOI: **10.1016/s1369-7021(03)00922-2**.

6 A. M. Abdalla, S. Hossain, O. B. Nisfindy, A. T. Azad, M. Dawood and A. K. Azad, Hydrogen production, storage, transportation and key challenges with applications: a review, *Energy Convers. Manage.*, 2018, **165**, 602–627, DOI: **10.1016/j.enconman.2018.03.088**.

7 B. Sarac, V. Zadorozhnyy, E. Berdonosova, Y. P. Ivanov, S. Klyamkin, S. Gumrukcu, A. S. Sarac, A. Korol, D. Semenov, M. Zadorozhnyy, A. Sharma, A. L. Greerd and J. Eckerta, Hydrogen storage performance of the multi-principal-component CoFeMnTiVZr alloy in electrochemical and gas-solid reactions, *RSC Adv.*, 2020, **10**, 24613–24623, DOI: **10.1039/d0ra04089d**.

8 H. H. Shen, X. T. Zu, B. Chen, C. Q. Huang and K. Sun, Direct observation of hydrogenation and dehydrogenation of a zirconium alloy, *J. Alloys Compd.*, 2016, **659**, 23–30, DOI: **10.1016/j.jallcom.2015.11.031**.

9 J. F. Zhang, Z. N. Li, Y. F. Wu, X. M. Guo, J. H. Ye, B. L. Yuan, S. M. Wang and L. J. Jiang, Recent advances on the thermal destabilization of Mg-based hydrogen storage materials, *RSC Adv.*, 2019, **9**, 408–428, DOI: **10.1039/c8ra05596c**.

10 A. Zaluska, L. Zaluski and J. O. Ström-Olsen, Synergy of hydrogen sorption in ball-milled hydrides of Mg and Mg2Ni, *J. Alloys Compd.*, 1999, **289**, 197–206, DOI: **10.1016/s0166-0462(99)00013-7**.

11 A. Jain, R. K. Jain, G. Agarwal and I. P. Jain, Crystal structure, hydrogen absorption and thermodynamics of $Zr_{1-x}Co_xFe_2$ alloys, *J. Alloys Compd.*, 2007, **438**, 106–109, DOI: **10.1016/j.jallcom.2006.08.007**.

12 J. W. Yeh, S. K. Chen, S. J. Lin, J. Y. Gan, T. S. Chin, T. T. Shun, C. H. Tsau and S. Y. Chang, Nanostructured High-Entropy Alloys with Multiple Principal Elements: Novel Alloy Design Concepts and Outcomes, *Adv. Energy Mater.*, 2004, **6**, 299–303, DOI: **10.1002/adem.200300567**.

13 B. Cantor, I. T. H. Chang, P. Knight and A. J. B. Vincent, Microstructural development in equiatomic multicomponent alloys, *Mater. Sci. Eng., A*, 2004, **375–377**, 213–218, DOI: **10.1016/j.msea.2003.10.257**.

14 B. Gludovatz, A. Hohenwarter, D. Catoor, E. H. Chang, E. P. George and R. O. Ritchie, A fracture-resistant high-entropy alloy for cryogenic applications, *science*, 2014, **345**, 1153–1158, DOI: **10.1126/science.1254581**.

15 Y. Liu, K. Wang, H. Xiao, G. Chen, Z. P. Wang, T. Hu, T. W. Fan and L. Ma, Theoretical study of the mechanical properties of $CrFeCoNiMo_x$ ($0.1 \leq x \leq 0.3$) alloys, *RSC Adv.*, 2020, **10**, 14080–14088, DOI: 10.1039/d0ra00111b.

16 P. Koželj, S. Vrtnik, A. Jelen, S. Jazbec, Z. Jagličić, S. Maiti, M. Feuerbacher, W. Steurer and J. Dolinšek, Discovery of a Superconducting High-Entropy Alloy, *Phys. Rev. Lett.*, 2014, **113**, 107001, DOI: 10.1103/physrevlett.113.107001.

17 C. P. Lee, Y. Y. Chen, C. Y. Hsu, J. W. Yeh and H. C. Shih, The Effect of Boron on the Corrosion Resistance of the High Entropy Alloys $Al_{0.5}CoCrCuFeNiB_x$, *J. Electrochem. Soc.*, 2007, **154**, C424–C430, DOI: 10.1149/1.2744133.

18 M. M. Nygård, G. Ek, D. Karlsson, M. Sahlberg, M. H. Sørby and B. C. Hauback, Hydrogen storage in high-entropy alloys with varying degree of local lattice strain, *Int. J. Hydrogen Energy*, 2019, **44**, 29140–29149, DOI: 10.1016/j.ijhydene.2019.03.223.

19 M. Sahlberg, D. Karlsson, C. Zlotea and U. Jansson, Superior hydrogen storage in high entropy alloys, *Sci. Rep.*, 2016, **6**, 36770, DOI: 10.1038/srep36770.

20 K. R. Cardoso, V. Roche, A. M. Jorge Jr, F. J. Antiqueira, G. Zepon and Y. Champion, Hydrogen storage in MgAlTiFeNi high entropy alloy, *J. Alloys Compd.*, 2021, **858**, 158357, DOI: 10.1016/j.jallcom.2020.158357.

21 C. Zhang, A. Song, Y. Yuan, Y. Wu, P. L. Zhang, Z. P. Lu and X. P. Song, Study on the hydrogen storage properties of a TiZrNbTa high entropy alloy, *Int. J. Hydrogen Energy*, 2020, **45**, 5367–5374, DOI: 10.1016/j.ijhydene.2019.05.214.

22 Y. F. Kao, S. K. Chen, J. H. Sheu, J. T. Lin, W. E. Lin, J.-W. Yeh, S.-J. Lin, T.-H. Liou and C.-W. Wang, Hydrogen storage properties of multi-principal-component $CoFeMnTi_xV_yZr_z$ alloys, *Int. J. Hydrogen Energy*, 2010, **35**, 9046–9059, DOI: 10.1016/j.ijhydene.2010.06.012.

23 C. Zhang, Y. Wu, L. You, X. Z. Cao, Z. P. Lu and X. P. Song, Investigation on the activation mechanism of hydrogen absorption in TiZrNbTa high entropy alloy, *J. Alloys Compd.*, 2019, **781**, 613–620, DOI: 10.1016/j.jallcom.2018.12.120.

24 J. Montero, G. Ek, M. Sahlberg and C. Zlotea, Improving the hydrogen cycling properties by Mg addition in Ti-V-Zr-Nb refractory high entropy alloy, *Scr. Mater.*, 2021, **194**, 113699, DOI: 10.1016/j.scriptamat.2020.113699.

25 P. Edalati, R. Floriano, A. Mohammadi, Y. T. Li, G. Zepon, H. W. Li and K. Edalati, Reversible room temperature hydrogen storage in high-entropy alloy TiZrCrMnFeNi, *Scr. Mater.*, 2020, **178**, 387–390, DOI: 10.1016/j.scriptamat.2019.12.009.

26 R. Floriano, G. Zepon, K. Edalati, G. L. B. G. Fontana, A. Mohammadi, Z. L. Ma, H. W. Li and R. J. Contieri, Hydrogen storage properties of new A_3B_2-type TiZrNbCrFe high-entropy alloy, *Int. J. Hydrogen Energy*, 2021, **46**, 23757–23766, DOI: 10.1016/j.ijhydene.2021.04.181.

27 F. Aouaini, N. Bouazizi, M. M. Almoneef, H. Al-Ghamdia and A. B. Lamine, Absorption and desorption of hydrogen in $Ti_{1.02}Cr_{1.1}Mn_{0.3}Fe_{0.6}RE_{0.03}$: experiments, characterization and analytical interpretation using statistical physics treatment, *RSC Adv.*, 2021, **11**, 15905–15920, DOI: 10.1039/d1ra00999k.

28 Z. W. Chen, X. Z. Xiao, L. X. Chen, X. L. Fan, L. X. Liu, S. Q. Li, H. W. Ge and Q. D. Wang, Influence of Ti super-stoichiometry on the hydrogen storage properties of $Ti_{1+x}Cr1.2Mn0.2Fe0.6$ (x = 0-0.1) alloys for hybrid hydrogen storage application, *J. Alloys Compd.*, 2014, **585**, 307–311, DOI: 10.1016/j.jallcom.2013.09.141.

29 C. Zlotea, M. A. Sow, G. Ek, J.-P. Couzinié, L. Perrière, I. Guillot, J. Bourgon, K. T. Møller, T. R. Jensen, E. Akiba and M. Sahlberg, Hydrogen sorption in TiZrNbHfTa high entropy alloy, *J. Alloys Compd.*, 2019, **775**, 667–674, DOI: 10.1016/j.jallcom.2018.10.108.

30 I. Kunce, M. Polanski and J. Bystrzycki, Microstructure and hydrogen storage properties of a TiZrNbMoV high entropy alloy synthesized using Laser Engineered Net Shaping (LENS), *Int. J. Hydrogen Energy*, 2014, **39**, 9904–9910, DOI: 10.1016/j.ijhydene.2014.02.067.

31 S. K. Dewangan, V. K. Sharma, P. Sahu and V. Kumar, Synthesis and characterization of hydrogenated novel AlCrFeMnNiW high entropy alloy, *Int. J. Hydrogen Energy*, 2020, **45**, 16984–16991, DOI: 10.1016/j.ijhydene.2019.08.113.

32 K. B. Zhang, Z. Y. Fu, J. Y. Zhang, W. M. Wang, H. Wang, Y. C. Wang, Q. J. Zhang and J. Shi, Microstructure and mechanical properties of $CoCrFeNiTiAl_x$ high-entropy alloys, *Mater. Sci. Eng., A*, 2009, **508**, 214–219, DOI: 10.1016/j.msea.2008.12.053.

33 S. Yang, F. Yang, C. L. Wu, Y. G. Chen, Y. Mao and L. S. Luo, Hydrogen storage and cyclic properties of $(VFe)_{60}(TiCrCo)_{40-x}Zr_x$ ($0 \leq x \leq 2$) alloys, *J. Alloys Compd.*, 2016, **663**, 460–465, DOI: 10.1016/j.jallcom.2015.12.125.

34 N. Yurchenko, N. Stepanov and G. Salishchev, Laves-phase formation criterion for high-entropy alloys, *Mater. Sci. Technol.*, 2017, **33**, 17–22, DOI: 10.1080/02670836.2016.1153277.

35 M. M. Nygård, G. Ek, D. Karlsson, M. H. Sørby, M. Sahlberg and B. C. Hauback, Counting electrons - A new approach to tailor the hydrogen sorption properties of high-entropy alloys, *Acta Mater.*, 2019, **175**, 121–129, DOI: 10.1016/j.actamat.2019.06.002.

36 D. B. Miracle and O. N. Senkov, A critical review of high entropy alloys and related concepts, *Acta Mater.*, 2017, **122**, 448–511, DOI: 10.1016/j.actamat.2016.08.081.

37 J. B. Mann, T. L. Meek and L. C. Allen, Configuration Energies of the Main Group Elements, *J. Am. Chem. Soc.*, 2000, **122**, 2780–2783, DOI: 10.1021/ja992866e.

38 J. B. Mann, T. L. Meek, E. T. Knight, J. F. Capitani and L. C. Allen, Configuration Energies of the d-Block Elements, *J. Am. Chem. Soc.*, 2000, **122**, 5132–5137, DOI: 10.1021/ja9928677.

39 A. Takeuchi and A. Inoue, Classification of Bulk Metallic Glasses by Atomic Size Difference, Heat of Mixing and Period of Constituent Elements and Its Application to Characterization of the Main Alloying Element, *Mater. Trans.*, 2005, **46**, 2817–2829, DOI: 10.2320/matertrans.46.2817.

40 T. M. Yue, H. Xie, X. Lin, H. O. Yang and G. H. Meng, Solidification behaviour in laser cladding of AlCoCrCuFeNi high-entropy alloy on magnesium substrates, *J. Alloys Compd.*, 2014, **587**, 588–593, DOI: 10.1016/j.jallcom.2013.10.254.